

Analysis of multi-angular data to retrieve indicators of ecosystem structure

Jean-Luc Widlowski^a, Bernard Pinty^a, Nadine Gobron^a, Michel M. Verstraete^a
and Anthony B. Davis^b

^aJoint Research Centre, Via E. Fermi, 1, Ispra, 21020 (VA), Italy

^bLos Alamos National Laboratory, Los Alamos, NM 87545, USA.

ABSTRACT

Vegetation structure significantly impacts the degree of anisotropy of the scattered radiation field. The proper analysis of multiangular data, such as those provided by the Multi-angle Imaging SpectroRadiometer (MISR) instrument on board Terra, could thus in principle yield statistical information on the structure of the observed environment. Preliminary investigation in this direction suggests that useful information on the heterogeneity of the vegetation can be retrieved at the subpixel scale.

Keywords: Multi-angular optical remote sensing, surface heterogeneity

1. INTRODUCTION

Retrieving information on the state of terrestrial vegetation canopies at the subpixel scale has either been approached through linear combinations of the spectral reflectances of two or more homogeneous end-members,¹ or, by pre-computing the reflectance fields of an ensemble of likely surface types using explicit three-dimensional radiation transfer models². Pinty et al.³ recently showed that the analysis of multi-angular reflectance data in the red spectral domain may yield information about the heterogeneity of the surface at the sensor subpixel scale. This approach is exploited by Gobron et al.⁴ to retrieve information on vegetation activity and structure from the Multi-angle Imaging SpectroRadiometer (MISR) instrument⁵ on board the NASA Terra platform. In the present work, this radiatively derived surface heterogeneity indicator k will be related to actual vegetation canopy height fields as characterized by their first-order structure-function⁶ and singularity measure⁷ exponents.

2. INTERPRETATION OF THE ANISOTROPY OF SURFACE-LEAVING RADIANCE FIELDS

All surfaces, natural or man-made, show some degree of spectral anisotropy when illuminated by a point source of light in the solar domain, *i.e.*, the Bidirectional Reflectance Factors (BRFs) of these media vary with both the illumination and observation directions⁸. This is because the measured BRF signal within the instantaneous field of view (IFOV) of the observing instrument condition the measured BRF signal through occlusion and mutual shading effects that alter the contributions of the scattering elements. Surface anisotropy thus provides an additional source of information and understanding the radiative processes that lead to these BRF observations should for a better characterisation of the observed geophysical system (see for instance Ref. 9).

Surface anisotropy patterns can be adequately represented by suitable parametric models. These models do not need to be based on or rigorously follow from basic physical principles, to the extent that they must only be able to mimic the anisotropy effects from a large variety of media in the simplest possible manner, that is with a minimum number of input parameters¹⁰. The RPV model,¹¹ a recent adaptation of a much older model rooted in planetary sciences, proposes a representation of the BRF fields on the basis of four* parameters ($k, \Theta, \rho_0, \rho_c$) entering a product of angular functions:

Further author information: (Send correspondence to Jean-Luc Widlowski)

Jean-Luc Widlowski: E-mail: Jean-Luc.widlowski@jrc.it, Telephone: +39 0332 78 9663, Fax +39 0332 78 9073

*The hot-spot parameter ρ_c is commonly set equal to the amplitude parameter ρ_0 , thus making the model effectively dependent on only three parameters.

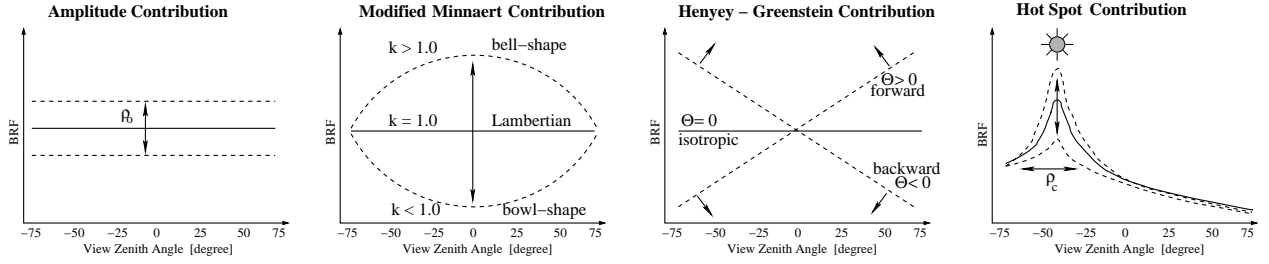


Figure 1. The RPV model performs a functional decomposition of any BRF field into an amplitude function (controlled by the ρ_0 parameter), a modified Minnaert function (controlled by the k parameter), a Henyey-Greenstein function (controlled by the Θ parameter), and a hot spot function (controlled by the ρ_c parameter). The modified Minnaert function contributes towards the ‘bowl’ and ‘bell’ shapedness, and the Henyey-Greenstein function towards the skewness of the resulting anisotropy shape.

$$\rho_{sfc}(z_0, \Omega_0 \rightarrow \Omega; \rho_0, \rho_c, \Theta, k) = \rho_0 \check{M}_I(\theta_0, \theta; k) F_{HG}(g; \Theta) H(\rho_c; G) \quad (1)$$

where z_0 represents the reference height of the BRF measurement, and Ω_0 and Ω represent the direction of incoming and outgoing radiation, respectively. It can be seen that the RPV model splits a surface BRF (ρ_{sfc}) into its amplitude component ρ_0 , its associated (symmetric) $\check{M}_I(\theta_0, \theta; k)$ and (asymmetric) $F_{HG}(g; \Theta)$ angular shape functions, as well as a hot spot descriptor function $H(\rho_c; G)$. With the exception of the amplitude function, all other parameters of the RPV model affect the overall reflectance field non-linearly across the hemisphere of possible viewing conditions. The main effects of the RPV model parameters on the overall signal shape are schematically depicted in Figure 1. Of specific interest here is the so-called modified Minnaert’s function $\check{M}_I(\theta_0, \theta; k)$, which allows for the mathematical representation of the overall shape of the angular field through the parameter k :

$$\check{M}_I(\theta_0, \theta; k) = \frac{\cos^{k-1} \theta_0 \cos^{k-1} \theta}{(\cos \theta_0 + \cos \theta)^{1-k}} \quad (2)$$

where θ_0 and θ represent the zenith angles of the incoming and outgoing directions, respectively. More specifically, k is close to 1.0 for a quasi Lambertian surface (very limited angular variations in the spectral BRF field), k is lower than 1.0 when a bowl-shaped reflectance pattern dominates (the spectral BRF values increase with the view zenith angle) and, conversely, k is greater than 1.0 when a bell-shaped reflectance pattern is observed (the spectral BRF values decrease with the view zenith angle). The RPV model was extensively evaluated by Engelsen¹² and can be inverted in a fast and reliable manner as demonstrated in a recent article by Gobron and Lajas¹³. Their approach yields not only an ensemble of possible RPV parameter value combinations but also the accuracy with which these k , Θ and ρ_0 parameters are capable of representing the observed BRF fields. Furthermore, a ‘‘most likely’’ parameter set is normally selected by identifying the k and Θ values that are associated with the ρ_0 closest to the mean of the retrieved amplitude values.

Pinty et al.¹⁴ showed that maps of the parameter k derived from an analysis of broadband METEOSAT data exhibit spatially consistent fields and features corresponding to known gradients in surface types which may or may not be represented by variations in the amplitude component of the BRF fields. This strongly suggests that the parameter k can be used as one additional and possibly independent source of information to better discriminate between various surface types than is feasible on the sole basis of spectral measurements. It is thus important to understand how the anisotropic signature of geophysical media can be interpreted and, in particular, what practical information could be derived from simple parameterizations such as the one used here.

2.1. Anisotropy pattern as an indicator of surface heterogeneity

The vast majority of terrestrial surfaces, whose anisotropy patterns have been investigated using laboratory, field, or airborne measurements, exhibit a bowl-shape anisotropy pattern. Models describing the scattering of light by homogeneous plane-parallel turbid geophysical media also typically generate this type of anisotropy pattern. Indeed, under such conditions, radiative transfer theory and, in particular, the multiple scattering component, predicts an increase of the BRF values together with the exiting zenith angle. This situation is also generally observed for closed (large values of the leaf area index) and structurally homogeneous plant canopies, bare soils and other planetary surfaces as well. Occasionally, however, the inverse pattern, that is a bell-shaped anisotropy, has been observed^{15,16}. It is thus interesting to investigate under which conditions the latter type of anisotropy occurs. A class of geophysical systems that exhibit a higher reflectance when observed from above than at large zenith angles can easily be conceived, especially at red wavelengths where the anisotropy pattern of the solar radiation field is largely controlled by the physical properties and geometric arrangement of the elements that constitute the terrestrial surface. Consider, for example, a sparse coniferous forest over a snow-covered field, or sparse bushes over a bright sandy desert. In these cases, the high background reflectance dominates at small observation zenith angles, while the absorbing properties of the dark vegetation control the reflectance of the entire scene/IFOV at large angles. These BRF fields should therefore exhibit a bell-shape pattern corresponding to k values greater than 1.0 when analyzed with the RPV model.

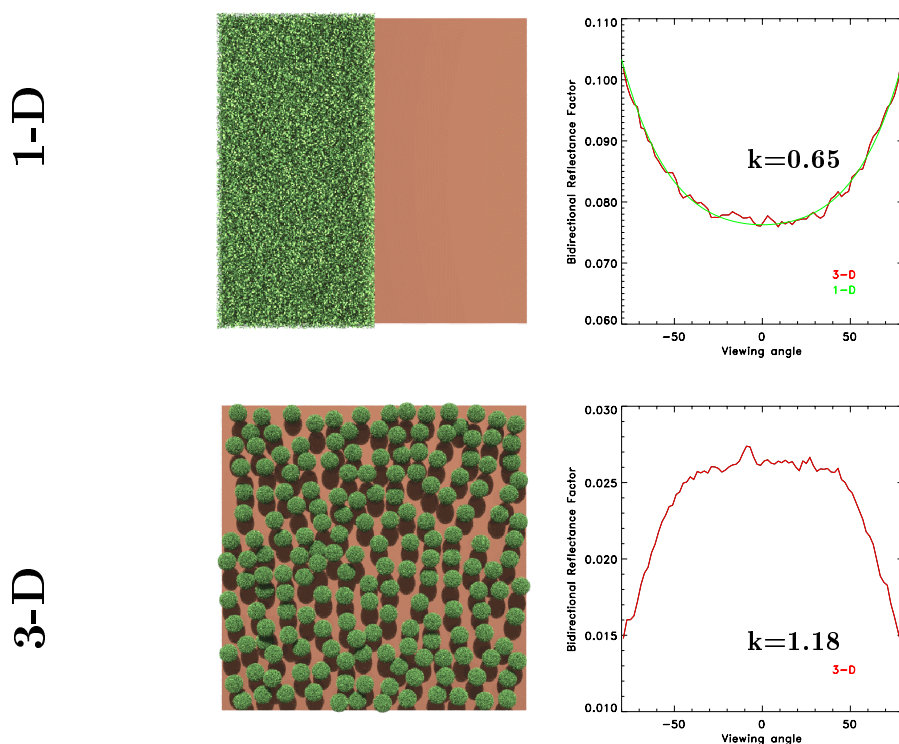


Figure 2. Typical angular signatures of the BRF field in the red spectral region emerging from quasi one-dimensional (top panels) and three-dimensional (bottom panel) vegetation scenes. Both scenes are composed of identical leaf and soil materials exhibiting exactly the same radiometric properties in the two experiments. The scene leaf area index is equal to 4 in both cases. The left panels provide an artistic view of the scenes and the right panels show the corresponding BRF field derived from model calculations in the cross-plane. In the right panels, the red (green) lines correspond to the BRF generated by the 3-D (1-D) model.

Figure 2 illustrates the differences between a quasi one-dimensional and a complex three-dimensional radiative transfer regime in the red spectral domain, and highlights the significant impact of canopy structure. The top panels provide a visualization of a simulated quasi one-dimensional scene (top left) together with the

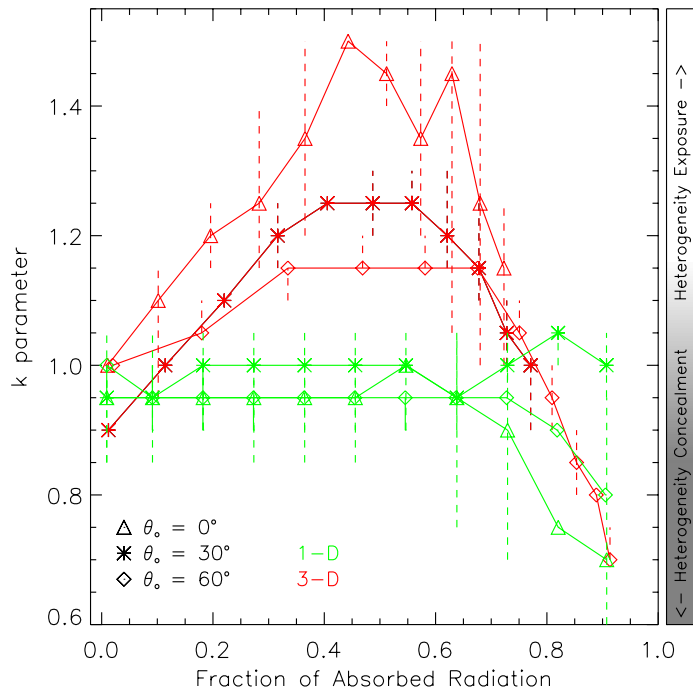


Figure 3. Variations of the k parameter values as a function of the fraction of absorbed radiation for Sun zenith angle equal to 0° (triangles), 30° (stars) and 60° (diamonds), respectively. Results obtained for the quasi one-dimensional and the corresponding three-dimensional scenes are identified with green and red colors, respectively. The vertical bars indicate the range of possible values for the k parameter that can provide an acceptable fit to the modelled BRF in each case.

corresponding BRF values generated in the cross plane (top right), *i.e.*, the plane perpendicular to the principal plane. These BRF values are calculated using a Monte-Carlo ray-tracing model developed by Govaerts and Verstraete¹⁷ (red line) and the model from Gobron et al.¹⁸ applicable for one-dimensional horizontally infinite canopy scenes (green line). In the latter case, the total BRF field emerging from the scene is approximated with a linear mixing of the respective contributions due to the vegetated and bare soil domains composing the scene. It follows the Independent Pixel Approximation (IPA) scheme proposed by Cahalan et al.¹⁹ in the case of cloud scenarios. In the top-left panel of Figure 2, the leaves are concentrated and grouped in one part of the scene and, thus, the complex interactions between the 3-D canopy and the soil are limited to the single straight boundary separating these two media in the horizontal plane. By contrast, the bottom-left panel of Figure 2 shows a geophysical situation where the three-dimensional effects are enhanced due to the regrouping of the leaves into clumps scattered throughout the scene. In this architecturally more complex scenario, the BRF values are accurately estimated using the Monte-Carlo ray-tracing model²⁰. It is noteworthy that the only difference between the two scenarios lies in the spatial distribution of the leaves in the scene, *i.e.*, the Leaf Area Index (LAI), the spectral and geometrical properties of the leaves and the soil are all set at the same values in both experiments.

To assess how the Minnaert function parameter k_{red} changes with increasing vegetation coverage in the case of structurally 1-D (green) and 3-D (red) scenarios—similar to those depicted in the left hand panels of Figure 2—the RPV model was inverted against BRF simulations of surface types having LAI values ranging from 0.5 to 5. Figure 3 shows the mean and the associated uncertainty values obtained for the parameter k when the fractional vegetation cover of the scene/IFOV (expressed in terms of the absorbed radiation fraction) is gradually increased from 1 to 100% under three different illumination conditions. It can be seen that:

1. too sparse a 3-D vegetation system does not systematically lead to $k > 1.0$ conditions because there is not enough vegetation to compensate, at large view zenith angles, for the BRF increase due to the illuminated

soil in between the vegetation elements. Such situations may, therefore, be almost indistinguishable from a plane-parallel (1-D) system, in the sense that the BRF fields estimated with the IPA are extremely close to those obtained with the full three-dimensional model, except in the vicinity of the hot spot angular region,

2. too dense (closed) a 3-D vegetation system does also hardly translate into a $k > 1.0$ estimation because the surface heterogeneity is not significant enough to create a detectable BRF increase signature at angles close to nadir, *i.e.*, the latter is masked by the shadowing effects,
3. only at intermediate densities of the 3-D vegetation system does one observe $k > 1.0$ conditions. Variations in the spectral and architectural properties of the vegetation attributes may yield different relationships between the leaf area index of the scenes and the values of the parameter k .

The same result holds for different Sun angle conditions as can be seen from Figure 3, where the values of the parameter k_{red} decrease with an increase of the Sun zenith angle from 0° to 30° and 60° : the reflectance of the background soil between the vegetation clumps becomes dominated by shadows and cannot deliver large BRF values even for viewing conditions close to nadir. Thus Figure 3 shows that when the illumination angle becomes as high as 60° , the projected clump shadows are significant enough to reduce the large values of the k_{red} parameter that would normally be associated with heterogeneous structures, for the spectral and architectural conditions prescribed in these simulations. By contrast, the quasi 1-D scenes are characterized by values which are always close to the $k = 1.0$ critical threshold, and under these conditions, the scene heterogeneity remains concealed.

The conjecture is thus that the observed bell-shaped anisotropy is often associated with the presence of vertically distributed absorbing material (*e.g.*, vegetation at the red wavelength because of the presence of strongly absorbing chlorophyll bands) overlying a brighter (more reflecting or less absorbing) interface or lower boundary condition (*e.g.*, the vast majority of soils at the red wavelength). Actual situations are of course very complex: the reflectance of each pixel of a heterogeneous system viewed from the nadir depends on competing factors such as the intrinsic optical properties of the scene elements but also the presence of shadows induced by the vertical stands. In fact, bell-shaped anisotropy patterns have been observed in the red spectral domain with both the MISR and AirMISR²¹ instruments. As can be seen in Figure 4, for example, the appearance of such (blue) $k > 1$ features is not haphazard but occurs in a spatially organised manner, suggesting that surface structural features may be the underlying reasons for these patterns. Indeed, when Pinty et al.³ conducted a field campaign at this Konza prairie site, they found that the values of $k > 1$ (derived from the atmospherically corrected BRF field) corresponded to surface targets containing vertical (vegetation) structures of medium density and bright underlying soils. Such situation included for example, a dry riverbed with tall bushes on both sides, a clearing in a wooded field with bare soil underneath (due to overgrazing by cattle), as well as several young maize stands with the bare soil still visible between the plants.

Thus, based on the above radiative transfer simulations and the qualitative field evaluation of actual AirMISR data analysis, one can postulate that there is a genuine opportunity to detect, on the basis of the k parameter value, the occurrence of a class of heterogeneous targets; specifically those made up of sparsely distributed, dark and predominantly vertically oriented architectures over a bright background. Since such spectral contrasts often occur in nature, these findings open new opportunities to characterize the heterogeneity of terrestrial ecosystems at the sub-pixel level, for a range of scales. What is thus needed at this point, is the establishment of some quantitative link between the observed reflectance anisotropy shape, on the one hand, and the spatial heterogeneity of the vegetation architecture that gave rise to these observations on the other. To this effect we will introduce intermittency and non-stationarity measures and apply these indicators to vegetation canopy height transects acting as a proxy for the 3-D structure of the simulated scenes.

The concept of spatial heterogeneity permeates the fields of ecology and hydrology, most notably in conjunction with GIS or remote sensing applications²²⁻²⁴. Just like the concept of scale, spatial heterogeneity does not possess a single universal definition, although it is mostly related to the notion of spatial variability (which in

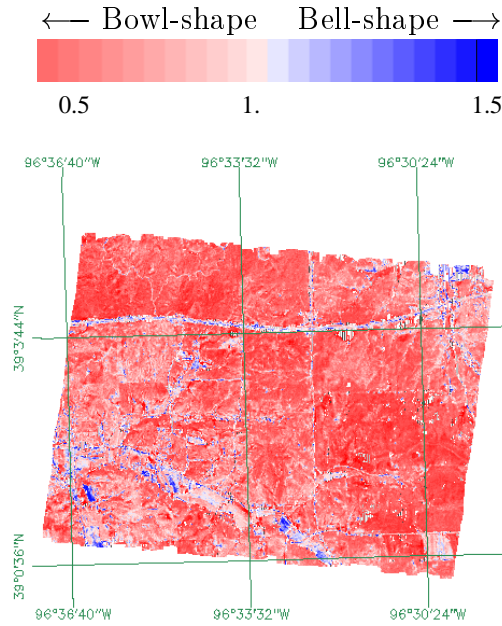


Figure 4. Map of the parameter k_{red} obtained from an inversion of the RPV model against “surface BRF” data collected in the red band of the AirMISR instrument over Konza prairie on July 13, 1999. This BRF dataset was derived using a simplified atmospheric transfer scheme. The color code goes from red tones for low k values to blue tones for large k values and the intermediate white colors indicate pixels exhibiting values close to unity for the parameter k .

turn is scale-dependent). In the context of point patterns, spatial heterogeneity means variations in the density of points (*e.g.*, tree positions in a forest), whereas from a surface pattern perspective it refers to the variability of a spatially continuous parameter²⁵. Alternatively spatial homogeneity might be defined as *remaining similar upon subdivision* which suggests the existence of a characteristic upper and lower limit of scales within which this property applies²⁶. In other words, both the resolution (or measurement interval), and the range (or sampling extent) determine the degree of spatial heterogeneity that can be associated with a specific data set. Changing any one of these two aspects may induce a change in the perceived degree of heterogeneity or homogeneity.

Fractals are conceptual objects that show structures at all spatial scales with a scale-independent self-similarity⁶. For example, a circle is not a fractal but a cloud is, since the latter does not become linear upon repeated magnification²⁶. The fractal dimension can be used as a quantifier for the roughness of a surface or data set. Recent studies have included measures of the fractal geometry of landscapes in patch pattern analyses such as soil and landscape data analysis, forest fire and cluster growth, tree and habitat structures as well as spatial habitat and landscape pattern analysis^{27–30}. In recent years the concept of multifractals^{7, 31, 32} have helped to clarify the fuzzy notion of inhomogeneity by introducing and quantifying the effects of intermittency³³. Whereas singularity analysis techniques^{34–36} allow for the extraction of the latter information, the more traditional structure function approach^{6, 37} constitutes a proper framework for addressing the non-stationarity behaviour of geophysical data or processes. In the following section both structure functions and singular analysis techniques will be introduced and subsequently combined for the characterization of geophysical data or processes in terms of their non-stationarity and intermittency properties, respectively^{33, 38–40}.

3. CHARACTERISATION OF VEGETATION STRUCTURE

A property of fundamental importance to data analysis is the notion of statistical homogeneity, or *stationarity*, that is defined as invariance of the statistical properties under translation. When this condition is not verified, no meaningful (stable) spatial statistics may be derived from a given data set, or even ensembles of data sets if

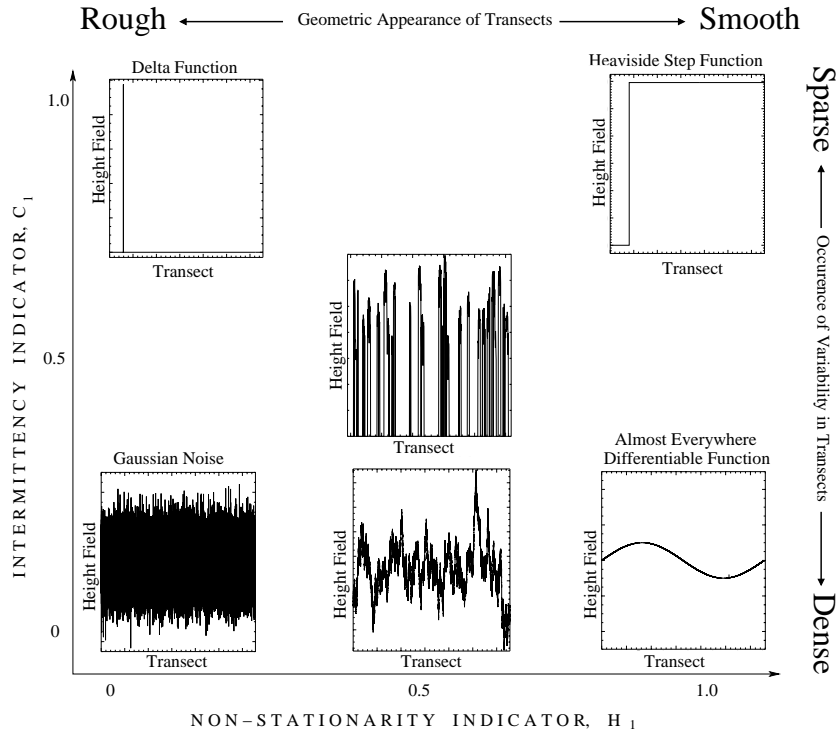


Figure 5. Conceptual $H_1 - C_1$ graph: Both Gaussian noise and randomly positioned Dirac δ functions appear geometrically rough and thus are stationary signals. Heaviside step functions and functions that are (varying and) differentiable almost everywhere appear geometrically smooth and hence non-stationary. The Heaviside step function and the Dirac δ function are characterized by highly singular occurrence of variability, *i.e.*, high intermittency. Gaussian noise, fractional Brownian motion and functions that are differentiable almost everywhere possess variability (between adjacent datapoints) almost everywhere, *i.e.*, low intermittency.

the spatial statistics of the latter do not converge to their ensemble average values, that is, if they violate ergodicity⁴¹. Stationarity can be linked to the geometric appearance of (one-dimensional) datasets, with *smooth*-looking transects being more non-stationary than *rough*-looking ones. To characterize the (non-)stationarity properties of a dataset, structure function analysis, or more specifically, the first order exponent of this technique (H_1) can be utilized. However, statistical stationarity is not a sufficient criteria for the unambiguous characterisation of geophysical datasets. Hence, to overcome this limitation the degree of intermittency (*i.e.*, the occurrence of larger than average jumps) can be quantified in geophysical datasets. Intermittency properties can also be related to the geometric appearance of (one-dimensional) datasets: Transects with a high degree of intermittency are characterized by relatively *sparse* occurrences of variability between adjacent datapoints, whereas for transects with a low degree of intermittency the occurrence of variability is rather *dense*. Intermittency can be characterized by singularity analysis, or more specifically by the first order exponent of this technique (C_1).

Figure 5 is an adaptation from Ref. 33 and provides a conceptual classification of various data transects in terms of their non-stationarity and intermittency properties. Stationary and non-intermittent Gaussian noise is positioned at (0,0). It's integral—Fractional Brownian motion—is non-intermittent but also somewhat non-stationary (0.5,0). Functions that are (varying and) differentiable almost everywhere occur around (1,0). Random Dirac Delta functions are highly intermittent but stationary processes (0,1). Heaviside step functions on the other hand are both non-stationary and highly intermittent constructs (1,1). In subsections 3.1 and 3.2 the procedures for computing both H_1 (structure function analysis) and C_1 (singularity analysis) will be described in greater detail. In section 4 actual vegetation canopy height fields will then be characterized using these two indicators.

3.1. Structure-function analysis

We consider a generic geophysical signal $\phi(x)$ that represents the “field” we are interested in. Furthermore we assume that $\phi(x)$ is sampled at intervals of length ℓ along the segment $[0, L]$:

$$\phi_i = \phi(x_i) \quad x_i = i\ell \quad i = 0, 1, \dots, \Lambda - 1$$

with the number of data points $\Lambda = (L + \ell)/\ell \gg 1$. Next, it is assumed that the geophysical signal behaves in a scale-invariant manner over a range of scales $\eta \leq r \leq R$, that is, power laws will prevail for all scale-conditioned statistics within this range. Thus, for a scale-invariant signal, free of characteristic scales, the corresponding energy spectrum $E(k)$ is expected to follow:

$$E(k) \propto k^{-\beta}$$

where the wavenumber, $k = 1/r$. Ref. 41 have shown that $\beta < 1$ implies stationarity, whereas $1 < \beta < 3$ relates to non-stationarity in geophysical fields that could however be stationary over some range of scales, $\eta \leq r \leq R$. In the following, only the latter type of geophysical signals are considered, and the absolute increment across the scale $r_j = j\ell$ with $j = 1, \dots, \Lambda - 1$ is defined as:

$$|\Delta\phi(r_j; x_i)| = |\phi(x_i + r_j) - \phi(x_i)| \quad i = 0, \dots, \Lambda - j - 1$$

which will be independent of position x_i due to the power-law behaviour. This obviously applies to all q -th order structure functions:

$$\langle |\Delta\phi(r_j)|^q \rangle = \frac{1}{\Lambda - j} \sum_{i=0}^{\Lambda-j-1} |\Delta\phi(r_j; x_i)|^q$$

where $\langle \cdot \rangle$ indicates ensemble averaging over all possible positions ($0 \leq x_i \leq L - r_j$) within the dataset. Due to the scale-invariance it can be expected that for $\eta \leq r \leq R$:

$$\langle |\Delta\phi(r)|^q \rangle \propto r^{\zeta(q)} \quad q \geq 0 \quad (3)$$

with $\zeta(q)$ being concave[†] as long as the proportionality factors in equation 3 depend only weakly³² on q . Furthermore, it is also non-decreasing if the increments $\Delta\phi(r_j; x_i)$ are bounded,^{42, 43} and finally, due to normalisation one has: $\zeta(0) = 0$. Thus, given the concavity of $\zeta(q)$ a hierarchy of non-increasing exponents $H(q)$ can be defined³⁸:

$$H(q) = \frac{\zeta(q)}{q} \quad q \geq 0$$

Obtaining $H(q)$ is the goal of the structure function analysis. Processes with a constant $H(q)$ are called “monoaffine” or “non-stationary monofractals” whereas those with a variable $H(q)$ are called “multiaffine” or “non-stationary multi-fractals”^{43, 44}. At least two $\zeta(q)$ are well known: For non-stationary scaling processes with stationary increments the second order structure function $\langle |\Delta\phi(r)|^2 \rangle$ —which is also known as the variogram in geostatistics—can be related to the slope of the power spectrum using the Wiener-Khintchine theorem³⁷:

$$1 \leq \beta = \zeta(2) + 1 = 2H(2) + 1 < 3$$

[†]A twice differentiable function $f(x)$, is *concave* (over the interval X) if its second derivative is nonpositive, and is *convex* if its second derivative is nonnegative (for all x within the interval X).

Furthermore, the $q = 1$ structure function can be related to the fractal dimension $D_{g(\phi)}$ of the graph $g(\phi)$ of $\phi(x)$, when the latter is being viewed as an object in two dimensional Euclidean space⁴⁵:

$$0 \leq H_1 = H(1) = \zeta(1) = 2 - D_{g(\phi)} \leq 1 \quad (4)$$

H_1 , which is known as the “roughness” or “Hurst” exponent, is thus bounded in the range $[0, 1]$. At its lower limit, H_1 relates to graph filling ($D_{g(\phi)} = 2$) stationary processes whilst at $H_1 = 1$ it indicates the presence of non-fractal signals that are differentiable almost everywhere ($D_{g(\phi)} = 1$)⁴³. Additionally, H_1 , which is also known as the codimension of $g(\phi)$, allows for a geometric interpretation of the data set under study: Low values ($H_1 \rightarrow 0$) relate to increased roughness in the signal whereas high values ($H_1 \rightarrow 1$) indicate the presence of smoothness. According to Davis et al.,⁴⁶ H_1 constitutes the single most important exponent in the whole $H(q)$ hierarchy, not necessarily because of the geometric significance of equation 4 but due to the fact that H_1 defines the linear trend in $\zeta(q)$ (compare with the right hand panel in Figure 6). In summary, these authors view H_1 as a direct quantifier of the system’s overall non-stationarity whereas the complete hierarchy of $\zeta(q)$ or $H(q)$ exponents may serve as a means to qualify the details of this non-stationarity. As such H_1 will provide one of the information axes when classifying the height-field structure of vegetation canopies in section 4 where this information will be related to the radiation field that emerges from within these surface types.

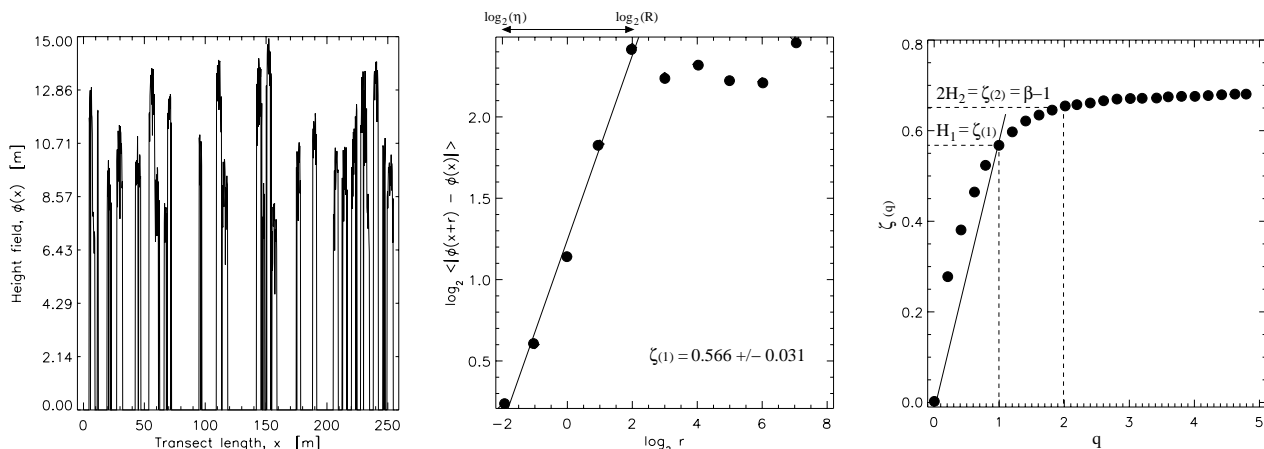


Figure 6. Left hand panel: A tree height transect corresponding to a scene with LAI=2.5 that is structurally equivalent to those in the bottom left panel of Figure 2 and that was sampled at ~ 25 cm interval over the nominal resolution of MISR (275 m). Middle panel: The corresponding \log_2 - \log_2 plot of the first order structure function versus the scale r . Right hand panel: The resulting $\zeta(q)$ function plotted against q with H_1 being indicated.

Figure 6 provides an overview of the structure function analysis: The left hand panel shows a tree height transect (corresponding to a 3-D scene with a LAI of 2.5 and being structurally equivalent to the scenes in the bottom left panel of Figure 2) sampled at ~ 25 cm interval over the spatial sampling frequency of MISR (275 m); the middle panel displays the corresponding \log_2 - \log_2 plot of the first order structure function versus the scale r ; and in the right hand panel the resulting $\zeta(q)$ function is plotted against q .

3.2. Singularity analysis

Although structure functions can be used to characterize the non-stationary multifractal structure of geophysical data-sets, such information is, however, not necessarily unique – especially for multifractal processes when only H_1 is being considered. In order to remove this indetermination it has been suggested to characterize the role of *intermittency* in the observed signal⁴⁰. In other words, it would be of interest to analyze the occurrence of “spikiness” (or larger-than-average jumps) – ideally in a stationary dataset. One way to obtain a stationary field from a non-stationary one with stationary increments ($1 < \beta < 3$) is by computing nearest-neighbour

differences⁴¹. This operation reduces the power spectrum slope of the resulting (absolute) gradient field β^* by two *i.e.*, $\beta^* = \beta - 2$. For the dataset in Figure 6 with $\beta \approx 1.65$, such an approach yields irregular gradient fields with $\beta^* < 0$, which does, however, not make a difference to the outcome of the singularity analysis^{47,48}. The “singular measures” approach of Davis et al.³⁸ and Marshak et al.⁴⁰ will be presented here, although other approaches have been proposed³⁴⁻³⁶.

The m -th order normalized absolute gradient field $\epsilon(\eta; x_i)_m$, is defined over the smallest scale (η) for which a power-law behaviour persists within the dataset (compare with Figure 6):

$$\epsilon(\eta; x_i)_m = \frac{|\Delta\phi(\eta; x_i)|^m}{\langle |\Delta\phi(\eta; x_i)|^m \rangle} \quad i = 0, 1, \dots, \Lambda - e - 1$$

where the scale $\eta = e\ell$ with (integer) $e > 0$, the number of data points $\Lambda = (L + \ell)/\ell \gg 1$ and ℓ is the sampling interval of the data points along the segment $[0, L]$. Also:

$$\langle |\Delta\phi(\eta; x_i)|^m \rangle = \frac{1}{\Lambda - e} \sum_{i=0}^{\Lambda-e-1} |\Delta\phi(\eta; x_i)|^m$$

Setting $m = 1$ for simplicity, the normalized absolute gradient field can be “coarse grained” for any position $0 \leq x \leq L - \eta - r$ and scale $0 \leq r \leq L - \eta$:

$$\epsilon(r_j; x_i) = \frac{1}{j+1} \sum_{i=i}^{i+j} \epsilon(\eta; x_i) \quad \begin{array}{l} i = 0, \dots, \Lambda - e - j - 1 \\ j = 0, \dots, \Lambda - e - 1 \end{array} \quad (5)$$

which when raised to the q -th power, before being averaged over all possible positions ($i = 0, \dots, \Lambda - e - j - 1$) along the normalized absolute gradient field, yields:

$$\langle \epsilon(r_j)^q \rangle = \frac{1}{\Lambda - e - j} \sum_{i=0}^{\Lambda-e-j-1} \epsilon(r_j; x_i)^q$$

These $\langle \epsilon(r_j)^q \rangle$ are presumably stationary and can be related (for some range of scales r) to the convex exponent function³⁵ $K(q)$:

$$\langle \epsilon(r)^q \rangle \propto \left(\frac{r}{L} \right)^{K(q)} \quad q \geq 0 \quad (6)$$

where the restriction on q is in general required only when some $\epsilon(\eta; x_i) = 0$ occur within the dataset⁴⁰. This was, however, the case for the height field transect shown in the left hand panel of Figure 6. Under such conditions a discontinuity in $K(q)$ may occur as $q \rightarrow 0$ (compare with the right hand panel in Figure 7). It is important to note that the scale ratio $r/L \ll 1$ in the small scale limit, which is always the most reliable³⁸. Both $K(0)$ and $K(1)$ are equal to zero, which follows from the normalization of the probability distribution function for $\epsilon(r_j; x_i)$, and from equation 5 which implies that $\langle \epsilon(r_j) \rangle = 1$ and hence⁴⁰ $K(1) = 0$.

As was the case for structure functions, a non-decreasing hierarchy of exponents can be defined $C(q) = K(q)/(q - 1)$ which is related to the well-known non-increasing hierarchy of “generalized dimensions” $D(q)$, first introduced by Hentschel and Procaccia⁷ and Grassberger³¹ in the context of deterministic chaos theory:

$$C(q) = 1 + D(q) = K(q)/(q - 1) \quad (7)$$

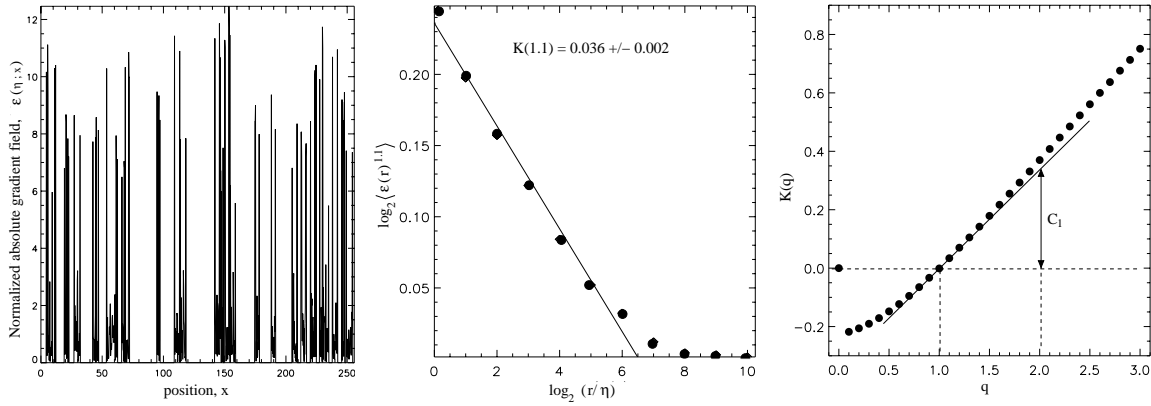


Figure 7. Left hand panel: The normalized absolute gradient field, $\epsilon(\eta; x)$ for the tree-height transect indicated in the left hand panel in Figure 6. Middle panel: The corresponding \log_2 - \log_2 plot of the $q = 1.1$ singularity measure, $\langle \epsilon(r)^{1.1} \rangle$ versus the scale r/η . Right hand panel: The resulting $K(q)$ function. Notice the discontinuity as $q \rightarrow 0$ and the quasi-linear increase beyond $q \approx 1.5$.

Given that $D(q)$ or $C(q)$ are constant, the process under study is termed “uniform” as opposed to “multifractal” if they are changing. Applying l’Hopital’s rule for $q \rightarrow 1$ in equation 7 yields a straightforward measure for the heterogeneity in the sense of singular measures, which is the currently accepted way of characterizing intermittency³⁸:

$$0 \leq C_1 = C(1) = K'(1) \leq 1$$

where the upper limit of C_1 has been set equal to 1 thus excluding degenerate gradient fields. At $C_1 = 0$ the data exhibits weak variability (low intermittency), whereas at its upper limit the signal becomes extremely intermittent (*e.g.*, random Dirac δ function). In the latter case, the signal may be characterized geometrically by the adjective ‘sparse’ whereas in the former, with information available almost everywhere along the data set *i.e.*, $D(1) = 1$, it may be labeled as ‘dense’. As was the case with structure functions, Davis et al.⁴⁶ argue that C_1 quantifies the essence of the intermittency whereas the full hierarchy of exponents is required to describe its details. Furthermore, they propose to utilize the $H_1 - C_1$ plane as a means of characterizing geophysical datasets when scale-invariance is present. Figure 5 displayed such a conceptual $\langle H_1 \rangle, \langle C_1 \rangle$ plane with the position of some specific data-sets being indicated. Note also that the central graph in this figure corresponds to the canopy height transect depicted in the left hand panel of Figure 6 with $C_1 \approx 0.37$ and $H_1 \approx 0.57$. In the following section the $H_1 - C_1$ approach will thus be applied to the characterisation of canopy height fields as a surrogate for the three-dimensional structure of vegetated surfaces. These structural statistics will then be related to the shape of the spectral reflectance anisotropy (as characterized by the Minnaert function parameter, k_{red}) that was simulated for these vegetation canopy types.

4. COMBINING SURFACE STRUCTURE AND REFLECTANCE INFORMATION

In order to derive the necessary canopy height data, the model of Govaerts and Verstraete¹⁷ was applied to a large variety of 3-D vegetation canopy representations. The sampling interval of the subsequent height measurements ($\ell \simeq 25$ cm), was chosen such as to be greater than the characteristic scale of the leaves, yet smaller than the typical dimension of the tree crowns or the gaps in between them. Some 40 transects of equal length (2^{10} data points) but with different origins and orientations were sampled. For each of these, the H_1, C_1 statistics were computed in the small scale limit following the approach of Davis et al.³⁸. The structure functions were fitted (on a \log_2 - \log_2 plot) from scale $\eta = \ell$ to the first detected scale break (~ 1 – 2 orders of magnitude), or, in its absence, through all the data. C_1 was computed from a normalized absolute gradient field of step size η . Ultimately, these H_1, C_1 statistics were ensemble-averaged to yield a directionally independent estimate of the

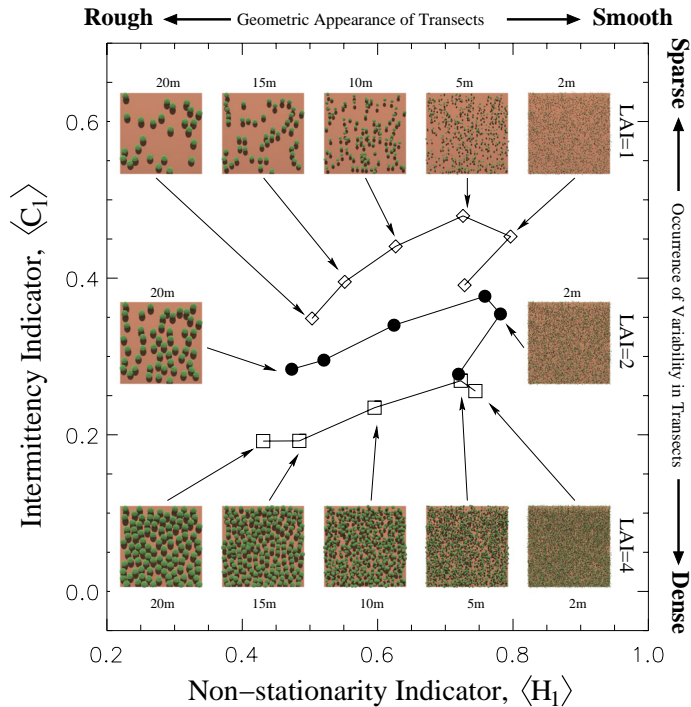


Figure 8. $\langle H_1 \rangle$, $\langle C_1 \rangle$ statistics for heterogeneous vegetation canopies composed of ‘floating’ spherical foliage clumps (with an LAI of 5). The diameter of the spherical envelopes is gradually increased from 1 m (right) to 20 m (left) to cover the scene with an overall LAI of 1 (diamonds), 2 (filled circles) and 4 (squares).

non-stationarity $\langle H_1 \rangle$ and intermittency $\langle C_1 \rangle$ of the vegetation height at the resolution of the MISR pixel (275 m). Figure 8 indicates the changes in H_1 , C_1 as the diameter of spherical foliage agglomerations (with a LAI of 5) is increased from 1 m to 20 m, to generate scenes with three different overall LAI values: 1 (diamonds), 2 (filled circles) and 4 (squares). It can be seen that the lower the scene-LAI the higher the value of the intermittency indicator C_1 . As the sphere size is decreased both H_1 and C_1 are increasing until, for sphere diameters smaller than ~ 5 m, the occurrence and size of “soil-to-tree jumps” is becoming too frequent on the one hand, and too regular on the other such that both indicators start to decrease again.

By simulating the surface leaving BRDF fields at the spatial resolution of MISR and subsequently inverting the RPV model against these data, the values of the Minnaert function parameter k_{red} can be retrieved for a large set of vegetation canopy architectures whose $\langle H_1 \rangle$, $\langle C_1 \rangle$ statistics are also known. Figure 9 shows that indeed, there exists an organisation in $\langle H_1 \rangle$, $\langle C_1 \rangle$ space of surface types with bell-shaped reflectance anisotropies ($k_{red} > 1.05$). It also shows that the size of this (blue coloured) cluster in $\langle H_1 \rangle$, $\langle C_1 \rangle$ space changes as the value of the solar zenith angle is altered from 0° (left panel) to 30° (right panel). Since the changes in the value of k_{red} are not uniform throughout $\langle H_1 \rangle$, $\langle C_1 \rangle$ space, multi-angular observations at different illumination conditions might be capable of providing the $\langle H_1 \rangle$, $\langle C_1 \rangle$ statistics of heterogeneous surface types (assuming the target does not change between observations).

These findings are promising since they support the earlier conjecture that the parameter k may contain structure information complementary to any spectrally-derived information (*e.g.*, the fraction of absorbed photosynthetically active radiation⁴). While a quantitative evaluation of the approach proposed here is underway, the usage of canopy height fields as a proxy for vegetation structure has the definite advantage that remote sensing techniques already exist to allow the measurement of these properties at sufficient high spatial resolutions^{49, 50}.

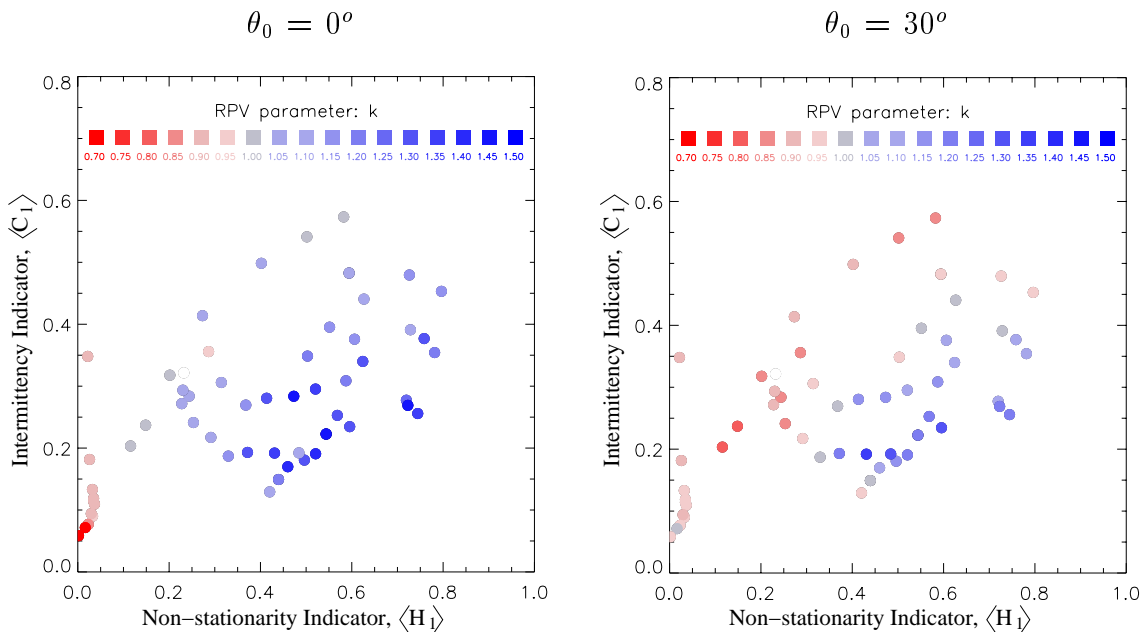


Figure 9. The Minnaert function parameter k_{red} (colour) in relation to the $\langle H_1 \rangle, \langle C_1 \rangle$ statistics for a series of surface types with the solar zenith angle being zero (left panel) and thirty degree (right panel).

5. CONCLUSION

It has been shown that vegetation canopy structure may be characterized in the small scale limit by non-stationarity $\langle H_1 \rangle$ and intermittency $\langle C_1 \rangle$ exponents using an ensemble of canopy height transects of different orientations and origins. More importantly, the reflectance anisotropy quantifier k , obtained by inversion of the parametric RVP model against multiangular terrestrial surface observations, when used in conjunction with the corresponding $\langle H_1 \rangle, \langle C_1 \rangle$ statistics, allows to identify specific types of vegetation that are characterized by medium-dense accumulations of vertically elongated foliage clumps. Therefore, if sufficient spectral contrast exists between the (darker) leaves and (brighter) ground cover in the red, k may be employed (in conjunction with spectral information and under appropriate sampling conditions) to characterize the underlying vegetation structure at the scale of the MISR subpixel resolution.

REFERENCES

1. R. Cahalan, W. Ridgeway, and W. J. Wiscombe, "Independent pixel and Monte Carlo estimates of stratocumulus albedo," *Journal of the Atmospheric Sciences* **51**, pp. 3776–3790, 1994.
2. J.-L. Widlowski, B. Pinty, N. Gobron, and M. M. Verstraete, "Detection and characterization of boreal coniferous forests from remote sensing data," *Journal of Geophysical Research* **106**, pp. 33,405–33,420, 2001.
3. B. Pinty, J.-L. Widlowski, N. Gobron, and M. M. Verstraete, "Uniqueness of multi-angular information - Part 1: A surface heterogeneity indicator from MISR," *IEEE Transactions on Geoscience and Remote Sensing* **40**, pp. 1560–1573, 2001.
4. N. Gobron, B. Pinty, M. M. Verstraete, J.-L. Widlowski, and D. J. Diner, "Uniqueness of multi-angular measurements - Part 2: Joint retrieval of vegetation structure and photosynthetic activity from MISR," *IEEE Transactions on Geoscience and Remote Sensing* **40**, pp. 1574–1592, 2002.
5. D. J. Diner, J. C. Beckert, T. H. Reilly, C. J. Bruegge, J. E. Conel, R. Kahn, J. V. Martonchik, T. P. Ackerman, R. Davies, S. A. W. Gerstl, H. R. Gordon, J. P. Muller, R. B. Myneni, P. J. Sellers, B. Pinty, and M. M. Verstraete, "Multiangle imaging spectroradiometer (MISR) description and experiment overview," *IEEE, Transactions on Geoscience and Remote Sensing* **36**, pp. 1072–1087, 1998.

6. B. B. Mandelbrot, *The Fractal Geometry of Nature*, W. H. Freeman, San Francisco, 1982.
7. H. G. E. Hentschel and I. Procaccia, "The infinite number of generalized dimensions of fractals and strange attractors," *Physica D* **8**, pp. 435–444, 1983.
8. J. V. Martonchik, C. J. Bruegge, and A. H. Strahler, "A review of reflectance nomenclature for remote sensing," *Remote Sensing Reviews* **19**, pp. 9–20, 2000.
9. N. Gobron, B. Pinty, M. M. Verstraete, J. V. Martonchik, and D. J. Diner, "The potential of multi-angular spectral measurements to characterize land surfaces: Conceptual approach and exploratory application," *Journal of Geophysical Research* **105**, pp. 17539–17550, 2000.
10. M. M. Verstraete, B. Pinty, and R. B. Myneni, "Potential and limitations of information extraction on the terrestrial biosphere from satellite remote sensing," *Remote Sensing of Environment* **58**, pp. 201–214, 1996.
11. H. Rahman, B. Pinty, and M. M. Verstraete, "Coupled surface-atmosphere reflectance (CSAR) model. 2. Semiempirical surface model usable with NOAA Advanced Very High Resolution Radiometer data," *Journal of Geophysical Research* **98**, pp. 20,791–20,801, 1993.
12. O. Engelsen, B. Pinty, M. M. Verstraete, and J. V. Martonchik, "Parametric bidirectional reflectance factor models: Evaluation, improvements and applications," Technical Report EUR 16426 EN, EC Joint Research Centre, 1996.
13. N. Gobron and D. Lajas, "A fast scheme to invert the RPV model against multiangle data," *Canadian Journal of Remote Sensing* **28**, pp. 156–167, 2002.
14. B. Pinty, F. Roveda, M. M. Verstraete, N. Gobron, Y. Govaerts, J. Martonchik, D. Diner, and R. Kahn, "Surface albedo retrieval from METEOSAT - Part 2: Application," *Journal of Geophysical Research* **105**, pp. 18113–18134, 2000.
15. F. F. Gerard and P. R. J. North, "Analyzing the effect of structural variability and canopy gaps on forest BRDF using a geometric-optical model," *Remote Sensing of Environment* **62**, pp. 46–62, 1997.
16. W. Ni and D. Jupp, "Spatial variance in directional remote sensing imagery - recent developments and future perspectives," *Remote Sensing Reviews* **18**, pp. 441–479, 2000.
17. Y. Govaerts and M. M. Verstraete, "Raytran: A Monte Carlo ray tracing model to compute light scattering in three-dimensional heterogeneous media," *IEEE Transactions on Geoscience and Remote Sensing* **36**, pp. 493–505, 1998.
18. N. Gobron, B. Pinty, M. M. Verstraete, and Y. Govaerts, "A semi-discrete model for the scattering of light by vegetation," *Journal of Geophysical Research* **102**, pp. 9431–9446, 1997.
19. R. F. Cahalan, W. Ridgway, W. J. Wiscombe, T. L. Bell, and J. B. Snider, "The albedo of fractal stratocumulus clouds," *Journal of Atmospheric sciences* **51**, pp. 2434–2455, 1994.
20. B. Pinty, N. Gobron, J.-L. Widlowski, S. A. W. Gerstl, M. M. Verstraete, M. Antunes, C. Bacour, F. Gascon, J.-P. Gastellu, N. Goel, S. Jacquemoud, P. North, W. Qin, and R. Thompson, "The RADIATION transfer Model Intercomparison (RAMI) exercise," *Journal of Geophysical Research* **106**, pp. 11937–11956, 2001.
21. D. J. Diner, L. M. Barge, C. J. Bruegge, T. G. Chrien, J. E. Conel, M. L. Eastwood, J. D. Garcia, H. M. A., C. G. Kurzweil, W. C. Ledebauer, P. N. D., C. M. Sarture, and B. G. Smith, "The airborne multi-angle imaging spectroradiometer AirMISR instrument description and first results," *IEEE, Transactions on Geoscience and Remote Sensing* **36**, pp. 1339–1349, 1998.
22. M. G. E. Turner, *Landscape heterogeneity and disturbance*, Springer-Verlag, New York, 1987.
23. J. Kolasa and S. T. E. Pickett, *Ecological Heterogeneity*, Springer-Verlag, New York, 1991.
24. J. D. Kalma and M. E. Sivapalan, *Scale issues in hydrological modelling.*, John Wiley & Sons, London, 1995.
25. P. Dutilleul, "Spatial heterogeneity and the design of ecological field experiments," *Ecology* **74**, pp. 1646–1658, 1993.
26. M. W. Palmer, "Fractal geometry: A tool for describing spatial patterns of plant communities," *Vegetatio* **75**, pp. 91–102, 1988.
27. R. H. Gardner, B. T. Milne, M. G. Turner, and R. V. O'Neill, "Neutral models for the analysis of broadscale landscape patterns," *Landscape Ecology* **1**, pp. 19–28, 1987.
28. M. F. Goodchild and D. M. Mark, "The fractal nature of geographic phenomena.," *Annals, Association of American Geographers* **77**, pp. 265–278, 1987.

29. B. T. Milne, "Measuring the fractal geometry of landscapes," *Applied Mathematics and Computation* **27**, pp. 67–79, 1988.
30. B. Zeide, "Fractal geometry in forestry applications," *Forest Ecology and Management* **46**, pp. 179–188, 1991.
31. P. Grassberger, "Generalized dimensions of strange attractors," *Physical Review Letters A* **97**, pp. 227–230, 1983.
32. G. Parisi and U. Frisch, "A multifractal model of intermittency," in *Turbulence and Predictability in Geophysical Fluid Dynamics*, M. Ghil, R. Benzi, and G. E. Parisi, eds., pp. 84–88, North Holland, Amsterdam, 1985.
33. A. B. Davis, A. L. Marshak, and W. J. Wiscombe, "Bi-multifractal analysis and multi-affine modelling of non-stationary geophysical processes, application to turbulence and clouds," *Fractals* **1**, pp. 560–567, 1993.
34. C. Meneveau and K. R. Sreenivasan, "The multifractal spectrum of the dissipation field in turbulent flows," *Nuclear Physics B* **2**, pp. 49–76, 1987.
35. D. Schertzer and S. Lovejoy, "Physical modelling and analysis of rain and clouds by anisotropic scaling and multiplicative processes," *Journal of Geophysical Research* **92**, pp. 9693–9714, 1987.
36. A. B. Chhabra, C. Meneveau, R. V. Jensen, and K. R. Sreenivasan, "Direct determination of the $f(\alpha)$ singularity spectrum," *Physical Review A* **40**, pp. 5284–5294, 1989.
37. A. S. Monin and A. M. Yaglom, *Statistical Fluid Mechanics: Mechanics of Turbulence*, MIT Press, London, 1975.
38. A. B. Davis, A. Marshak, W. J. Wiscombe, and R. F. Cahalan, "Multifractal characterization of nonstationarity and intermittency in geophysical fields: Observed, retrieved, or simulated," *Journal of Geophysical Research* **99**, pp. 8055–8072, 1994.
39. A. B. Davis, A. Marshak, H. Gerber, and W. J. Wiscombe, "Horizontal structure of marine boundary layer clouds from centimeter to kilometer scales," *Journal of Geophysical Research* **104**, pp. 6123–6144, 1999.
40. A. Marshak, A. Davis, W. Wiscombe, and R. F. Cahalan, "Scale invariance in liquid water distributions in marine stratocumulus. Part II: Multifractal properties and intermittency issues," *Journal of the Atmospheric Sciences* **54**, pp. 1423–1444, 1997.
41. A. B. Davis, A. Marshak, W. J. Wiscombe, and R. F. Cahalan, "Scale invariance in liquid water distributions in marine stratocumulus. Part I: Spectral properties and stationarity issues," *Journal of the Atmospheric Sciences* **53**, pp. 1538–1558, 1996.
42. U. Frisch, "From global scaling à la Kolmogorov, to local multifractal in fully developed turbulence," *Proceedings of The Royal Society London, section A* **434**, pp. 89–99, 1991.
43. A. Marshak, A. Davis, R. Cahalan, and W. Wiscombe, "Bounded cascade models as nonstationary multifractals," *Physical Review E* **49**, pp. 55–69, 1994.
44. T. Viscek and A.-L. Barabási, "Multi-affine model for the velocity distribution in fully developed flows," *Journal of Physics A: Mathematics and General* **24**, pp. L845–851, 1991.
45. B. B. Mandelbrot, *Fractals: Form, Chance, and Dimension*, W. H. Freeman, San Francisco, 1977.
46. A. B. Davis, A. Marshak, and W. J. Wiscombe, "Wavelet-based multifractal analysis of non-stationary and/or intermittent geophysical signals," in *Wavelets in Geophysics*, E. Foufoula-Georgiou and P. Kumar, eds., pp. 249–298, Academic Press, San Diego, 1994.
47. D. Lavallée, D. Schertzer, S. Lovejoy, and P. Ladoy, "Nonlinear variability and simulation of landscape topography," in *Fractal in geography*, L. De Cola and M. Lam, eds., pp. 158–192, Kluwer, Amsterdam, 1993.
48. Y. Tessier, S. Lovejoy, and D. Schertzer, "Universal multifractals: Theory and observations for rain and clouds," *Journal of Applied Meteorology* **32**, pp. 223–250, 1993.
49. M. A. Lefsky, W. B. Cohen, G. G. Parker, and D. J. Harding, "Lidar remote sensing for ecosystem studies," *BioScience* **52**, pp. 19–30, 2002.
50. R. N. Treuhaft and P. R. Siquera, "The vertical structure of vegetated land surfaces from interferometric and polarimetric radar," *Radio Science* **35**, pp. 141–177, 2000.